Draft version March 5, 2024
Preprint typeset using LaTeX style emulateapj v. 05/12/14

SCALING RELATIONS OF STARBURST-DRIVEN GALACTIC WINDS

Ryan Tanner, Gerald Cecil, and Fabian Heitsch
University of North Carolina at Chapel Hill
Chapel Hill, NC 27599-3255
rjtanner@physics.unc.edu

Draft version March 5, 2024

ABSTRACT

Using synthetic absorption lines generated from 3D hydro-dynamical simulations we explore how the velocity of a starburst-driven galactic wind correlates with the star formation rate (SFR) and SFR density. We find strong correlations until the scaling relations flatten abruptly at a point set by the mass loading of the starburst. Below this point the scaling relation depends on the temperature regime being probed by the absorption line, not on the mass loading. The exact scaling relation depends on whether the maximum or mean velocity of the absorption line is used. We find that the outflow velocity of neutral gas is four to five times lower than the average velocity of the hottest gas, the difference increasing with gas ionization. Thus, absorption lines of neutral or low ionized gas will underestimate the outflow velocity of hot gas, severely underestimating outflow energetics.

Keywords: galaxies: evolution — galaxies: nuclei — galaxies: starburst — ISM: jets and outflows — galaxies: kinematics and dynamics — hydrodynamics

1. INTRODUCTION

Observations beginning in the 1990s established galactic winds as ubiquitous phenomena associated with star-forming galaxies (Heckman et al. 1993; Bland-Hawthorn 1995; Dahlem 1997; Heckman et al. 2000). These observations focused on optical emission lines images and spectroscopy (Heckman et al. 1993). Optical imagery established the physical morphology of galactic winds and spectroscopy provided the kinematics and warm plasma diagnostics. While emission traced the interaction of the warm ISM with the hot wind, absorption lines probed the interaction between warm and cold gas and the hot wind (Heckman et al. 2000). X-ray emission, first observed in M82 (Watson et al. 1984), would also become important for identifying galactic outflows and measuring wind energetics (Fabbiano 1988; Fabbiano et al. 1990; Heckman et al. 1993, 1995). While some studies of galactic winds focused on X-ray emission (Strickland & Stevens 2000; Strickland & Heckman 2009), Bland-Hawthorn (1995) predicted that multi-band observations of galactic winds would become standard in characterizing galactic winds, and Veilleux et al. (2005) have shown that subsequent multi-band studies are important in characterizing the galactic wind.

More recent observations (Martin et al. 2012; Arribas et al. 2014; Rubin et al. 2014; Chisholm et al. 2015; Heckman et al. 2015; Heckman & Borthakur 2016) show that galactic winds are ubiquitous for star forming galaxies. Galactic winds are detected in 45% (Martin et al. 2012), 74% (Chisholm et al. 2015), 66% (89% for face on, 45% for edge on galaxies) (Rubin et al. 2014), and 90% (Heckman et al. 2015; Heckman & Borthakur 2016) of star forming galaxies surveyed. Outflow kinematics are typically measured using UV absorption lines such as: Mg II and Fe II (Rubin et al. 2014), Si II, Si III, Si IV and O I (Chisholm et al. 2015; Ho et al. 2016; Heckman et al. 2015; Heckman & Borthakur 2016), Na D (Heckman et al. 2000; Martin 2005), Hα and O III (Cicone et al. 2016), and C II and N II (Heckman et al. 2015; Heckman & Borthakur 2016).

Heckman et al. (2000) found that starburst galaxies whose Na D absorption line is dominated by the ISM, typically exhibited outflow velocities of > 100 km s^{-1}, with maximum velocities ranging from $300-700$ km s^{-1}. They were able to map outflow gas up to 10 kpc from the galactic center. They concluded that dense clouds in the ISM were being disrupted by the galactic wind, and that the ablated gas was being accelerated up to the terminal wind velocity.

Martin (2005) investigated the relationship between outflow velocities, as measured by the Na D lines, and the SFR. She found that the maximum wind velocity correlates as SFR$^{.35}$, and that stellar luminosity suffices to accelerate cool outflows to the terminal velocity. Martin noted that the covering fraction of the cold gas is not complete, which indicates that it is not a continuous fluid but is broken into clouds or shells.

Rubin et al. (2014) extended previous work using Mg II and Fe II absorption lines to find that outflows are detected for all $M_\star$, SFR and SFR density ($\Sigma_{\rm SFR}$) studied. Interestingly they found no evidence of a minimum threshold for $\Sigma_{\rm SFR}$. This indicates that galactic winds can still form in galaxies with extremely low $\Sigma_{\rm SFR}$. Although outflows were detected for all parameter ranges, a correlation was only found between outflow velocity and $M_\star$. These findings are both consistent with and conflict with previous work (Weiner et al. 2009; Chen et al. 2010; Heckman et al. 2011; Martin et al. 2012).

Conversely Chisholm et al. (2015) found correlations between $M_\star$ and SFR, but not with $\Sigma_{\rm SFR}$, using Si II absorption lines. They found a weak correlation between SFR and maximum velocity, but a slightly stronger correlation between SFR and the velocity as measured by the line center. In agreement with Rubin et al. (2014), Chisholm et al. (2015) found that there is no minimum $\Sigma_{\rm SFR}$ at which outflows form.

Cicone et al. (2016) studied a large sample of galaxies and found that the outflow velocity correlates with both

the SFR and the specific SFR, but only for a SFR $>$ 1 $M_\odot$ yr^{-1}.

Heckman et al. (2015) and Heckman & Borthakur (2016) found that the outflow velocity correlates strongly with SFR and Σ_{SFR} but weakly with galactic stellar mass. They also also noted that at sufficiently high Σ_{SFR} the correlation flattens out.

In this paper we resolve these differences and explain why some surveys of starburst galaxies have found correlations between the outflow velocity of starburst-driven winds and both SFR and Σ_{SFR}, while others have not. We also address why even among studies of star forming galaxies that have found a correlation, there is no agreement on the measured scaling relation. We use 3D hydro models of nuclear starbursts to study how the outflow velocities of galactic winds scale with SFR and Σ_{SFR}. In Section 2 we explain our setup and model parameters. In Section 3 we describe how we generate synthetic absorption profiles for Si ions to use as tracers of outflow velocity at different gas temperatures. In Section 4 we describe how the outflow velocity correlates with SFR and Σ_{SFR}, followed with a discussion in Section 5 of how our results relate to observational results.

2. SETUP

Our models use the setup of Tanner et al. (2016, hereafter Paper I) with a few modifications described below. As in Paper I we simulate a nuclear starburst inside a box 1000 pc on a side. The stellar gravitational potential and associated parameters are set to correspond to an M82 sized galaxy. All models are run for 1.5 Myr.

2.1. *Static Mesh Refinement*

In Paper I we employed a single grid, but in this paper we use the static mesh refinement (SMR) available in Athena (Stone et al. 2008). We use two levels of refinement covering the starburst and wind region directly above the starburst extending to the +z boundary, as shown in Figure 1. The base grid is divided into 64^3 cells, the first level divided into $64 \times 64 \times 112$ cells, and the second level divided into $128 \times 128 \times 160$ cells. This gives spatial resolution of 15.6 pc on the base grid and 7.8 and 3.9 pc on each respective level. The resolution of the top level corresponds to our medium resolution models from Paper I.

2.2. *Analytic Wind Velocity*

As in Paper I we model the starburst as a spheroidal region where we inject thermal energy ($\dot{E}$) and mass ($\dot{M}$) at each time step. The analytical wind velocity depends on both $\dot{E}$ and $\dot{M}$ as,

$$v_A = \sqrt{2\frac{\dot{E}}{\dot{M}}}. \quad (1)$$

In this paper and in Paper I we refer to v_A as the analytic wind velocity, whereas Veilleux et al. (2005); Strickland & Heckman (2009) refer to it as the terminal wind velocity. Both $\dot{E}$ and $\dot{M}$ are proportional to the total contribution from supernovae (SN) and stellar winds (SW) in the starburst. The total thermal energy injected into the ISM depends on the thermalization efficiency (ϵ), which

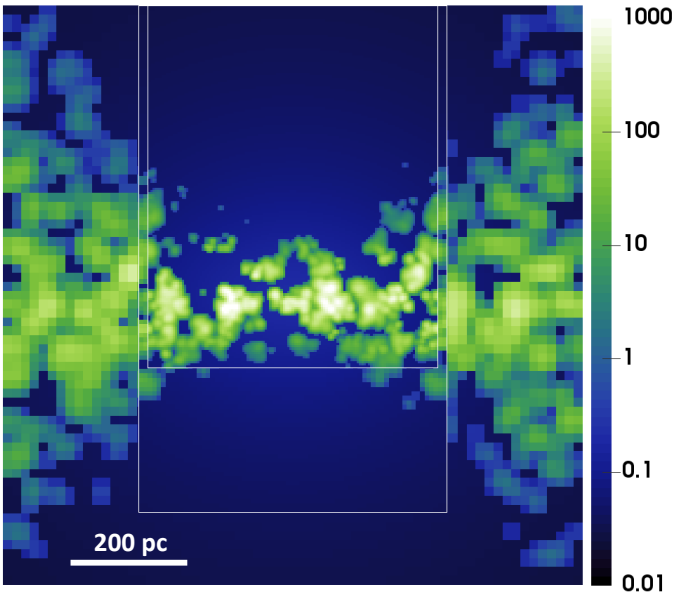

Figure 1. XZ plane slice of initial gas density (particles cm^{-3}) scaled logarithmically. White lines indicate SMR levels of refinement.

gives the fraction of SN and SW energy ($\dot{E}_{SN+SW}$) retained by the ISM as shown in Equation 2.

$$\dot{E} = \epsilon \dot{E}_{SN+SW} \quad (2)$$

The total mass added to the ISM by the starburst includes contributions from SN and SW ($\dot{M}_{SN+SW}$) and cold gas ($\dot{M}_{cold}$) remaining from star formation that cannot be resolved by our simulations. The additional mass from cold gas can be factored in as a scaling factor (β) for $\dot{M}_{SN+SW}$ and is referred to as the mass loading factor (Veilleux et al. 2005; Strickland & Heckman 2009), as shown in Equation 3.

$$\dot{M} = \dot{M}_{SN+SW} + \dot{M}_{cold} = \beta \dot{M}_{SN+SW} \quad (3)$$

We calculate $\dot{E}_{SN+SW}$ and $\dot{M}_{SN+SW}$ using Starburst99 models (Leitherer et al. 1999). We assume continuous star formation (CSF) with a Kroupa (2001) IMF, and Geneva stellar evolutionary tracks with solar metallicity. Both $\dot{E}_{SN+SW}$ and $\dot{M}_{SN+SW}$ scale with SFR (Veilleux et al. 2005) as,

$$\dot{E}_{SN+SW} = 4.324e41 \text{ (erg s}^{-1}\text{) SFR} \quad (4)$$

$$\dot{M}_{SN+SW} = 0.1902 \text{ (M}_\odot \text{ yr}^{-1}\text{) SFR.} \quad (5)$$

With the above assumptions $\dot{E}_{SN+SW}$ and $\dot{M}_{SN+SW}$ are constant after $\sim$ 5 Myr. Thus we assume the starburst begins CSF 5 Myr before the start of our simulations, and we run our simulations for 1.5 Myr by which time a steady state wind has formed. Inserting Equations 2, 3, 4, and 5 into Equation 1 and simplifying we get,

$$v_A = (1894 \text{ km s}^{-1})\sqrt{2\frac{\epsilon}{\beta}}. \quad (6)$$

Thus v_A does not depend on the SFR, but only ϵ and β. The actual velocity of the hot gas will be some fraction of v_A, and will be discussed in Section 4. We use v_A as a free parameter that we set in our models.

2.3. *Model Series*

We run two series of models, which we label series S and R, to test how the measured velocity of a galactic wind scales with the SFR and the SFR density ($\Sigma_{\rm SFR}$) respectively. For all models we set $\epsilon = 1.0$, v_A to 1000, 1500 or 2000 km s^{-1}, and use Equation 6 to calculate β.

The S series varies the SFR from 1 to 100 M$_\odot$ yr^{-1} in steps of 0.1 dex. For the S series we range over all SFRs with v_A set to 1000, 1500 or 2000 km s^{-1} (β = 7.1745, 3.1887, 1.7936 respectively) for a total of 63 models. As in Paper I, our S series uses a starburst radius of 150 pc. Model numbers denote first the v_A then the SFR. Thus model number S_15_79 has v_A = 1500 km s^{-1} and SFR = 7.9 M$_\odot$ yr^{-1}.

The R series varies the radius (r) of the starburst from 50 to 500 pc in steps of 0.1 dex. Each model in the R series has a fixed SFR of 10, 50 or 100 M$_\odot$ yr^{-1} for a total of 33 models. The SFR density for this series is calculated using, $\Sigma_{\rm SFR} = {\rm SFR}/\pi r^2$. All R series models use v_A = 2000 km s^{-1} (β = 1.7936). Model numbers denote first the SFR then the starburst radius. Thus model number R_50_79 has SFR 50 M$_\odot$ yr^{-1} and starburst radius 79 pc.

3. ABSORPTION PROFILES

To probe the outflow velocities of different temperature regimes we generate synthetic absorption profiles for various silicon ions. We generate our absorption profiles by calculating the optical depth in each cell for a set of velocity channels directly above the starburst ($z > 100$ pc) ranging from -2800 km s^{-1} to 200 km s^{-1}. We then integrate along a column of cells in the +z direction to get a total optical depth for each velocity channel, and then average each channel over all columns. We use a channel resolution of $\Delta v_{ch} = 0.25$ km s^{-1}.

The absorption coefficient for a single velocity channel (v_{ch}) is,

$$\kappa(v_{ch}) = N(v_{ch})a(v_{ch}) \tag{7}$$

where $N(v_{ch})$ is the column density and $a(v_{ch})$ is the absorption per atom. The column density is calculated from the cell density and the ionization fraction (Mazzotta et al. 1998). For simplicity, and to compare with observations (Chisholm et al. 2015; Heckman & Borthakur 2016), we choose to use silicon ions for our analysis. The ionization fractions for Si I-XIII in collisional ionization equilibrium and at various temperatures are shown in Figure 2.

Contributions from Doppler broadening and spontaneous radiative transitions $a(v_{ch})$ is given as,

$$a(v_{ch}) = \frac{\pi e^2}{m_e c}\frac{1}{\sqrt{\pi}}\frac{1}{\Delta\nu_{1/2}} f H(v_{ch}). \tag{8}$$

Here m_e is the mass of an electron, c is the speed of light, $\Delta\nu_{1/2}$ is the half width half maximum (HWHM) of the Gaussian component, f is the oscillator strength, and $H(v_{ch})$ is a Voigt profile. The Gaussian HWHM is calculated (Kwok 2007) using,

$$\Delta\nu_{1/2} = \frac{2}{c}\sqrt{\frac{2k_B T}{m}\ln(2)\nu_0} \tag{9}$$

with k_B Boltzmann's constant, T the gas temperature, m the atomic mass of the ion, and ν_0 the frequency of the line center from the NIST Atomic Spectra database (Kramida et al. 2015). We calculate the Voigt profile ($H(v_{ch})$) using Matlab code[1] written by Dr. Nikolay Cherkasov which employs the method of Schreier (2011).

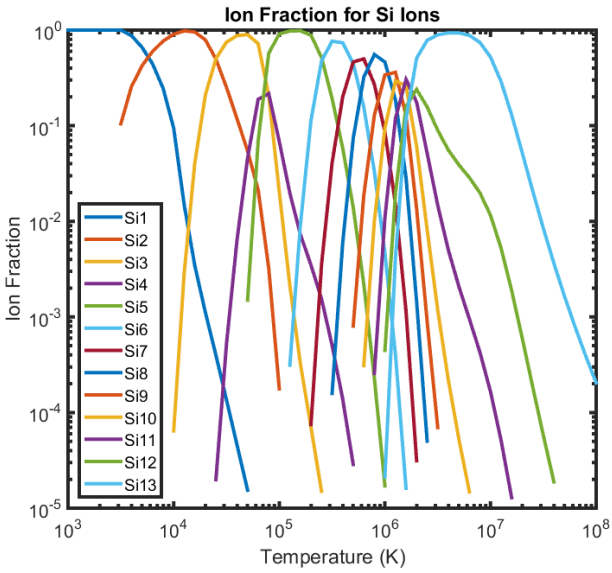

Figure 2. Ionization fractions for Silicon ions (Mazzotta et al. 1998) in collisional equilibrium at various temperatures.

We calculate a normalized Voigt profile for each cell and then Doppler shift the profile using the z velocity of the gas in the cell. The Doppler shift for each cell is calculated with respect to the systemic velocity of the galaxy, with negative velocities toward the observer and positive velocities away from the observer.

Using Equation 7 we calculate the optical depth of each cell

$$\tau_i(v_{ch}) = \kappa_i(v_{ch})dz. \tag{10}$$

The optical depth for each velocity channel is then summed along a column in the z direction. The intensity for each velocity channel is calculated using,

$$I(v_{ch}) = I_0(v_{ch})\mathrm{e}^{-\tau(v_{ch})}. \tag{11}$$

The resulting profile is then averaged over all columns directly over the starburst and then re-normalized so that we can compare the profiles of different ions. Figure 3 gives an example of a synthetic absorption profile for the Si IV line.

Using the synthetic absorption lines, we measure outflow velocities of each ion in two ways. v_{cen} is the velocity at half of the full width at half maximum (FWHM). This effectively measures the average outflow velocity for the temperature range of the ion. v_{90} is the velocity on the blueward side of the line where the absorption profile returns to 90% of full intensity. This measures the maximum velocity of the gas for a specific temperature range. These velocity measures were adopted by (Martin 2005; Weiner et al. 2009; Erb et al. 2012; Chisholm et al. 2015; Ho et al. 2016; Heckman & Borthakur 2016), while others have used different, but comparable velocity measures (Rupke et al. 2005; Bordoloi et al. 2014; Heckman

[1] http://www.mathworks.com/matlabcentral/fileexchange/45058-deconvolution-mordenite-zeolite

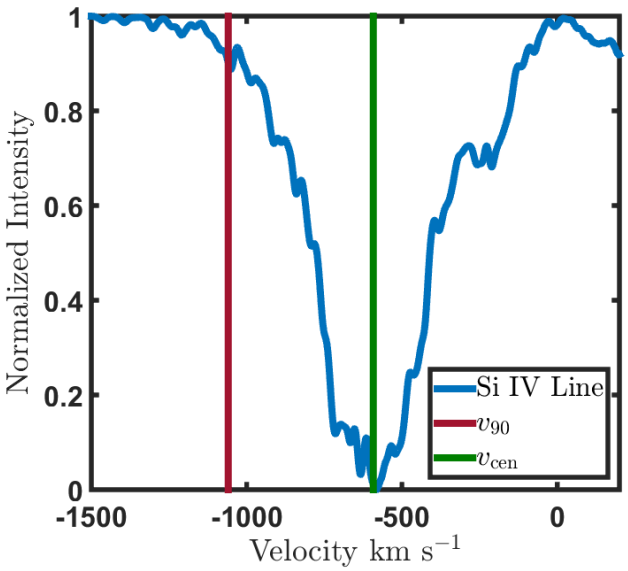

Figure 3. Synthetic absorption profile for a Si IV line. S_20_100 model with an analytic wind velocity of 2,000 km s^{-1} and a SFR of 10 M$_\odot$ yr^{-1}. Vertical lines indicate v_{cen} and v_{90} velocities.

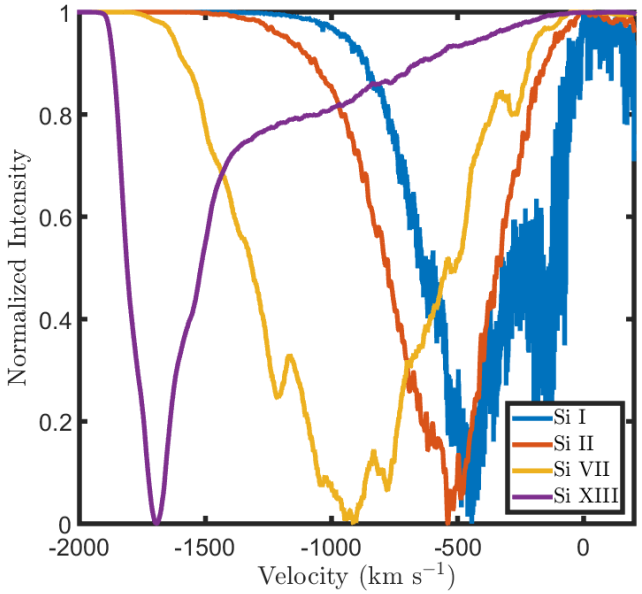

Figure 4. Synthetic absorption lines for Si I, II, VII, and XIII from my S_20_1000 model, which has a v_A of 2000 km s^{-1} and a SFR of 100 M$_\odot$ yr^{-1}.

et al. 2015; Cicone et al. 2016). We use these velocities to determine the relationship between the galactic wind and the properties of the starburst. The vertical lines in Figure 3 show v_{cen} and v_{90} for a synthetic absorption profile.

4. RESULTS

In this section we investigate the relationships between v_{cen} and v_{90}, and the analytic wind velocity (v_A from Equation 6), the SFR, and the SFR density (Σ_{SFR}). This allows us to determine how the outflow velocities of the multi-phase medium scale with different starburst properties.

4.1. *Outflow Velocities of Different Ions*

In Figure 4 we plot synthetic absorption lines for Si I, II, VII, and XIII for our S_20_1000 model. These four lines probe gas temperature ranges corresponding to $< 1e4$ K, $1e4 - 2.5e4$ K, $4.5e5 - 7e5$ K, and $2e6 - 1e7$ K respectively. We note that hotter, highly ionized gas has a higher outflow velocity. This is in accordance with our results in Paper I. For the Si XIII line $v_{\rm cen} \approx 1700$ km s^{-1}, and $v_{90} \approx 1900$ km s^{-1}. These values are slightly less than the $v_A = 2000$ km s^{-1} of the S_20_1000 model. This difference is due to energy lost to cooling and kinetic energy transferred to the surrounding ISM. The cold gas, traced by Si I, moves much slower with $v_{\rm cen} \approx 300$ km s^{-1}, and $v_{90} \approx 800$ km s^{-1}. The $v_{\rm cen}$ and v_{90} velocities for Si II are slightly higher than Si I, and the values for Si VII are midway between Si I and Si XIII.

To further determine how the velocity of the gas changes with increasing ionization we plot in Figure 5 (Subplots (a) and (b)) v_{cen} and v_{90} respectively for Si I-XIII from our S series models. The plots include models with v_A of 1000, 1500, and 2000 km s^{-1} at SFR of 10, 50, and 100 M$_\odot$ yr^{-1}.

We find three distinct velocity regimes corresponding to Si I-II, Si III-XI, and Si XII-XIII, which correspond to temperatures ranges $< 2.5e4$ K, $2.5e4 - 2e6$ K, and $> 2e6$ K, respectively. The outflowing gas in the cold regime has much lower $v_{\rm cen}$ and v_{90} than the warm regime, which in turn has lower velocities than the hot regime. In the warm regime the velocity plateaus and does not increase for several ions. For each ion, the measured velocity increases with increasing v_A, with a few notable exceptions. Models with $v_A = 1000$ km s^{-1} show little variation in velocities for different SFRs, and the increase in velocity for hotter gas is less pronounced and occurs at Si VIII instead of Si XII or Si XIII as with models with higher v_A. The measured velocities for all ions from our model with a SFR 10 M$_\odot$ yr^{-1} and $v_A = 1500$ km s^{-1} are lower than the velocities from models with higher SFRs and $v_A = 1500$ km s^{-1}. Our models with $v_A = 2000$ km s^{-1} show a similar trend.

In Figure 5 (Subplots (c) and (d)) we plot the v_{cen} and v_{90} velocities respectively for Si I-XIII from our R series models. A similar three part grouping of velocities in cold, warm and hot regimes is evident. For each ion there is a trend of increasing velocity for increasing $\Sigma_{\rm SFR}$.

4.2. *Scaling Relations*

4.2.1. *Outflow Velocity vs. SFR*

To see how the maximum and central velocities scale with SFR, in Figures 6 and 7 we plot v_{90} and $v_{\rm cen}$ respectively, versus SFR for Si I, II, IV and XIII from all S series models. The plots in Figure 6 show that the maximum outflow velocity is correlated with the SFR, but only for some SFRs depending on the v_A of the starburst. The measured v_{90} velocity resulting from cold or warm gas correlates with the SFR until the velocity reaches some fraction of v_A, and then the relationship flattens out. This effect is most clearly seen in the plot for Si IV lines (Figure 6 (c)). In the case of Si IV, the relationship flattens out when the v_{90} velocity is $\sim 80\%$ of v_A. A similar effect is observed for Si I and II v_{90} velocities, with a turnover in the relationship at $\sim 50\%$

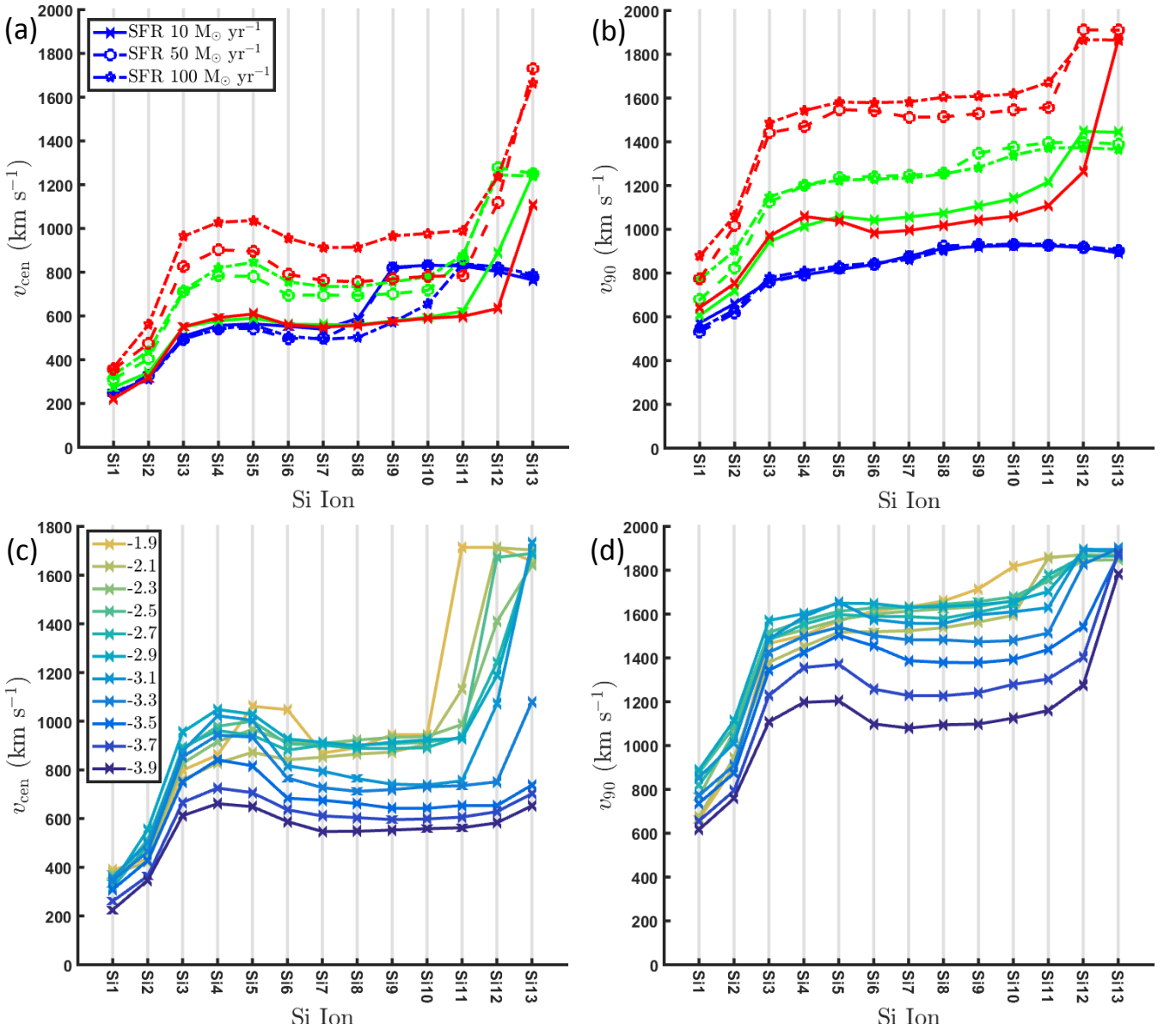

Figure 5. Outflow velocities of Si ions I-XIII for select S and R series models. Top, S series: Blue lines are for models with $v_A = 1,000$ km s^{-1}, green for $v_A = 1,500$, and red for $v_A = 2,000$. Solid lines with 'x' indicate models with SFR of 10 M$_\odot$ yr^{-1}, dashed lines with circles indicate a SFR of 50 M$_\odot$ yr^{-1}, and dot dashed lines with pentagrams indicate models with SFR of 100 M$_\odot$ yr^{-1}. (a) v_{cen} velocity of all Si ions. (b) v_{90} velocity of all Si ions. Bottom, R Series: Models have a SFR of 100 M$_\odot$ yr^{-1}. Numbers in legend indicate log($\Sigma_{\rm SFR}$) M$_\odot$ yr^{-1} pc^{-2} of the models. (a) v_{cen} velocity, (b) v_{90} velocity.

Table 1
Fit data for outflow velocities vs. SFR from S series models.
Only models below the turnover point are used.

Ion	Slope (δ)	Intercept (α)
v_{90} Velocities		
Si I	0.38 ± 0.08	2.37 ± 0.06
Si II	0.28 ± 0.06	2.56 ± 0.05
Si III	0.26 ± 0.03	2.72 ± 0.03
Si IV	0.25 ± 0.03	2.76 ± 0.03
$v_{\rm cen}$ Velocities		
Si I	0.28 ± 0.03	2.11 ± 0.03
Si II	0.32 ± 0.05	2.20 ± 0.04
Si III	0.34 ± 0.06	2.38 ± 0.05
Si IV	0.37 ± 0.08	2.39 ± 0.06

Table 2
Fit data for outflow velocities vs. $\Sigma_{\rm SFR}$ from R series models.
Only models below the turnover point are used.

Ion	Slope (δ)	Intercept (α)
v_{90} Velocities		
Si I	0.32 ± 0.07	4.0 ± 0.3
Si II	0.28 ± 0.05	3.9 ± 0.2
Si III	0.25 ± 0.05	4.0 ± 0.2
Si IV	0.22 ± 0.05	3.9 ± 0.2
$v_{\rm cen}$ Velocities		
Si I	0.35 ± 0.08	3.7 ± 0.3
Si II	0.26 ± 0.04	3.5 ± 0.1
Si III	0.32 ± 0.07	3.9 ± 0.3
Si IV	0.32 ± 0.07	4.0 ± 0.3

and $\sim 65\%$ of v_A respectively.

The scaling relationship for Si XIII is flat, indicating that there is no correlation between SFR and outflow velocity for the hot gas. This is in agreement with Equation 6, which shows that the analytic velocity does not depend on the the SFR. For hot gas, the v_{90} velocity is roughly constant at $\sim 90\%$ of v_A for all SFRs.

Figure 7 shows that there are similar scaling relations between $v_{\rm cen}$ and SFR. But the relationship flattens out at $\sim 20\%$, $\sim 30\%$ and $\sim 50\%$ of v_A for Si I, II and IV respectively. Interestingly, Si XIII now shows a correlation between SFR and the outflow velocity for low SFRs, with the relationship flattening out at $\sim 85\%$ of v_A.

We perform a fit to each set of models with the same v_A and then fit all models combined. The scaling relationship is of the form,

$$\log(v) = \delta \log(\mathrm{SFR}) + \alpha \tag{12}$$

For both v_{90} and $v_{\rm cen}$ the scaling relation with SFR is steepest for models with a $v_A = 2,000$ km s^{-1} and nearly flat for models with a $v_A = 1,000$ km s^{-1}. For example, using $v_{\rm cen}$ velocities from Si IV lines, $\delta = 0.35 \pm 0.08$ for models with $v_A = 2,000$ km s^{-1}, and $\delta = 0.14 \pm 0.08$ for models with $v_A = 1,000$ km s^{-1}. For all data combined the fit falls between those two extremes with $\delta = 0.25 \pm 0.04$. All uncertainties are reported at a 95% confidence level. The lower δ values are a result of including models with a SFR above the point where the relationship flattens out.

As can be seen in Figures 6 and 7, the same scaling relation exists for all models below the turnover point independent of v_A. We restrict our data set to models with SFRs below the turnover point and then fit the remaining data. The resulting slopes and y intercepts for these fits for v_{90} and $v_{\rm cen}$ are given Table 1. As can be seen in Table 1 for v_{90} the slope is higher for low ionization and decreases with increasing ionization. But for $v_{\rm cen}$ the slope is lower for low ionization and increases with increasing ionization. Thus colder gas has a greater δ value than warmer gas for v_{90}, while the opposite is true for $v_{\rm cen}$.

4.2.2. *Outflow Velocity vs. SFR Density*

Using our R series models we determine the relationship between the outflow velocity and the SFR density ($\Sigma_{\rm SFR}$). In Figure 8 we plot the v_{90} velocity versus $\Sigma_{\rm SFR}$ for all R series models. For our R series we set $v_A = 2000$ km s^{-1} and tested three SFRs (10, 50 and 100 M$_\odot$ yr^{-1}) while varying the size of the starburst to achieve a range of $\Sigma_{\rm SFR}$.

As can be seen in Figure 8, much like with Figure 6, the outflow velocity is correlated with $\Sigma_{\rm SFR}$, up to a point, and then the correlation flattens out. For all ions, including Si XIII, the turnover point for v_{90} is at $\log(\Sigma_{\rm SFR}) \approx -3.5$ (M$_\odot$ yr^{-1} pc^{-2}). The turnover point for $v_{\rm cen}$ is slightly higher at $\log(\Sigma_{\rm SFR}) \approx -3.0$ (M$_\odot$ yr^{-1} pc^{-2}). Because we set $v_A = 2000$ km s^{-1} for our R series these turnover points are higher than they would be for models with a lower v_A. As shown in Section 4.2.1, models with a lower v_A have a lower turnover point. If we compare the velocities at the turnover point for each ion in our R series we find that they are similar to the velocities at the turnover point for our S series models with $v_A = 2000$ km s^{-1}.

We perform a similar analysis as was done in Section 4.2.1 on our R series and determine scaling relations for models below the turnover point. The fit parameters are summed up in Table 2. Similar to our results for our S series, the slopes calculated using v_{90} velocities are steeper for colder gas and shallower for warmer gas. But the opposite trend between cold and warm gas slopes calculated using $v_{\rm cen}$ velocities is not as clear, since Si I produces the steepest slope.

It is interesting to note that the SFR does not affect the outflow velocity, even below the turnover point. In Figure 8 for each ion we plot three sets of models with different SFRs. There is significant overlap among the three sets, and all have similar scaling relations, turnover points, and velocities above the turnover point.

5. DISCUSSION

5.1. *Absorption Line Shape*

There are two important characteristics of our synthetic absorption profiles, the smoothness and the asymmetry of the lines. In Figure 4 the Si I line is not smooth, but has a large number of jagged spikes especially at lower velocities. As explained in Paper I, the colder gas entrained in the wind is confined in filamentary structures with lower velocity than the surrounding hot gas. As these filaments fragment in the wind due to Kelvin-Helmholtz instabilities they produce many dense cores (Cooper et al. 2009). The contributions from these dense cores embedded in the filaments produce the

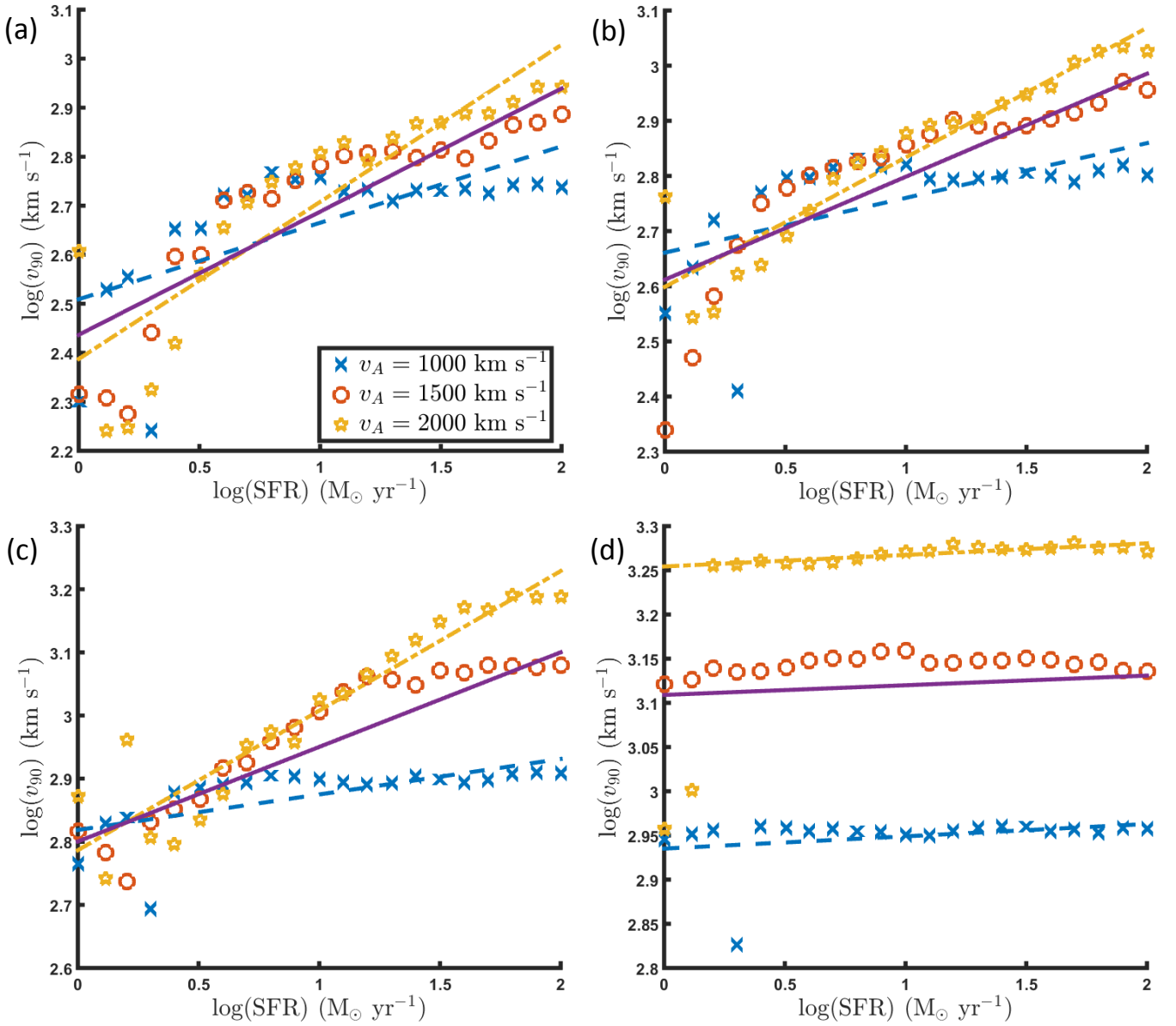

Figure 6. The v_{90} velocity vs SFR for all S series models for select Si ions: (a) Si I, (b) Si II, (c) Si IV, (d) Si XIII. Lines indicate linear fits for models with $v_A = 2000$ km s^{-1} (yellow, dot-dash line), $v_A = 1000$ km s^{-1} (blue, dashed line), and all models together (purple, solid line).

jagged shape of the Si I line. The smoothness of the absorption line, or lack thereof, reflects the distribution of vertical velocities of the dense cores and filaments. We note that there is measurable absorption at positive velocities from dense cores that have been elevated above the galactic disk but whose vertical movement has stalled.

The Si II line is significantly smoother than the Si I line. This indicate that the gas traced by the Si II line is significantly less clumpy than the colder gas traced by Si I. As the dense cores embedded in the wind are disrupted, the cold gas is ablated and accelerated to a higher velocity while being heated by the wind. This produces the asymmetric profiles of the Si I and II lines. These asymmetries have been observed in absorption lines from several galaxies (Grimes et al. 2009; Jones et al. 2012; Wofford et al. 2013; Heckman et al. 2015; Alexandroff et al. 2015; Chisholm et al. 2015, 2016). The asymmetric tail to higher velocities results from ablated gas being accelerated as it is entrained in the hot wind. The Si IV (Figure 3) and Si VII (Figure 4) lines are not highly asymmetric due to contributions from both slower gas ablated off of the cooler dense cores, and warmer gas beginning to mix with the hot gas that fills the superbubble created by the starburst. The Si VII line is not entirely smooth as it traces the large scale structure of filaments embedded in the wind. The asymmetry of the Si XIII line skews in the opposite direction. The long tail to lower velocities results from the hot gas being accelerated as it moves off the galactic disk. It reaches terminal velocity at ~ 300 pc above the galactic center to form the deep dip in absorption in Figure 4.

5.2. *Outflow Velocities*

As shown in Figures 6 and 7 the measured outflow velocity for neutral and slightly ionized gas increases with SFR. Considering just Si II (Subplot (b) in both Figures 6 and 7), at SFR $= 1$ M$_\odot$ yr^{-1}, $v_{\rm cen} \approx 160$ km s^{-1} and $v_{90} \approx 400$ km s^{-1}. At SFR $= 100$ M$_\odot$ yr^{-1} there is significant divergence in the measured velocities depending on the v_A, but the highest measured velocities are $v_{\rm cen} \approx 560$ km s^{-1} and $v_{90} \approx 1070$ km s^{-1}.

Chisholm et al. (2015) use Si II lines to measure outflow velocities from their sample of star forming galaxies with SFRs ranging from 0.01 M$_\odot$ yr^{-1} to 100 M$_\odot$ yr^{-1}. At SFR $= 1$ M$_\odot$ yr^{-1} they measure $v_{\rm cen} \approx 50$ to 150 km s^{-1} and $v_{90} \approx 350$ km s^{-1}. At higher SFRs they also have increased scatter in their measured velocities as we have in our data. At SFR $\lesssim 100$ M$_\odot$ yr^{-1} their highest velocities are $v_{\rm cen} \approx 500$ km s^{-1} and $v_{90} \approx 1100$ km s^{-1}. Thus our measured velocities correspond to the outflow velocities found by Chisholm et al. (2015). We find similar agreement with the measured velocities from Heckman et al. (2015) and Heckman & Borthakur (2016), but only for our models with the highest v_A.

The sample of galaxies used by Heckman et al. (2015) and Heckman & Borthakur (2016) overlap with the sample used by Chisholm et al. (2015), as both use data from Heckman et al. (2011) and Alexandroff et al. (2015), but the overlap only accounts for about a third to a half of the galaxies. This results in increased scatter in the measured velocities at higher SFRs for Heckman et al. (2015).

As shown in Figure 5 the velocities of neutral or slightly ionized gas are significantly lower than the velocity of the hot, highly ionized gas. Higher outflow velocities for higher ionization have been found in some surveys of starburst galaxies (Grimes et al. 2009; Cicone et al. 2016). Thus surveys which rely on absorption lines which trace neutral gas (Heckman et al. 2000; Martin 2005), or low ionized gas (Rubin et al. 2014; Chisholm et al. 2015; Heckman et al. 2015; Heckman & Borthakur 2016; Cicone et al. 2016) will underestimate outflow energetics.

The difference is more pronounced at low SFRs below the turnover point where there is degeneracy in the measured velocities for models with differing v_A. This difference is greatest for models with high v_A. The degeneracy below the turnover point means the degree to which the energy of the outflow is underestimated cannot be known. At higher SFRs above the turnover point, the velocity of neutral and low ionized gas can more reliably be used as a proxy for the outflow velocity of the hot gas.

5.3. *Scaling Relations*

A scaling relation between outflow velocity and SFR has been found in numerous surveys of starburst galaxies (Heckman et al. 2000; Martin 2005; Rupke et al. 2005; Weiner et al. 2009; Martin et al. 2012; Erb et al. 2012; Kornei et al. 2012; Bordoloi et al. 2014; Rubin et al. 2014; Chisholm et al. 2015, 2016; Heckman et al. 2015; Heckman & Borthakur 2016; Cicone et al. 2016). A similar relationship has been found between the outflow velocity and $\Sigma_{\rm SFR}$ (Chen et al. 2010; Kornei et al. 2012; Rubin et al. 2014; Chisholm et al. 2015, 2016; Heckman et al. 2015; Heckman & Borthakur 2016).

All of these surveys rely on either optical or UV absorption lines, which trace warm, not hot gas. Our results in Section 4.2.1 show that only the hot gas follows the relation given in Equation 6, where the outflow velocity does not depend on the SFR. The outflow velocity of the warm gas does depend on the SFR, but only if the velocity is below some fraction of v_A. The turnover point where the relationship flattens out, also called the saturation point (Heckman et al. 2015; Heckman & Borthakur 2016), depends on the v_A associated with the starburst and the ion being used. Below the turnover point the scaling relation for each ion is uniform and does not depend on v_A.

Many surveys find a correlation between outflow velocity and SFR, but there is no agreement about the slope of the scaling relation (δ). For example, using v_{90} velocities Rupke et al. (2005) find $\delta = 0.21$, Weiner et al. (2009) find $\delta = 0.38$, Chisholm et al. (2015) find $\delta = 0.081$, and Heckman & Borthakur (2016) find $\delta = 0.32$. Yet using $v_{\rm cen}$ velocities Martin (2005) find $\delta = 0.35$, and Chisholm et al. (2015) find $\delta = 0.22$.

Our results show that the lower δ values result from samples comprising a combination of galaxies with high and low v_A velocities, and therefore a mix of galaxies above and below the turnover point. Including a mix of galaxies in the sample would produce increased scatter in the data at higher SFRs or $\Sigma_{\rm SFR}$ because it would include galaxies above the turnover point in the relationship. In contrast, the higher δ values would come from samples of galaxies with either relatively uniform, and high, v_A, or a sample restricted to the lower range of SFRs below the turnover point.

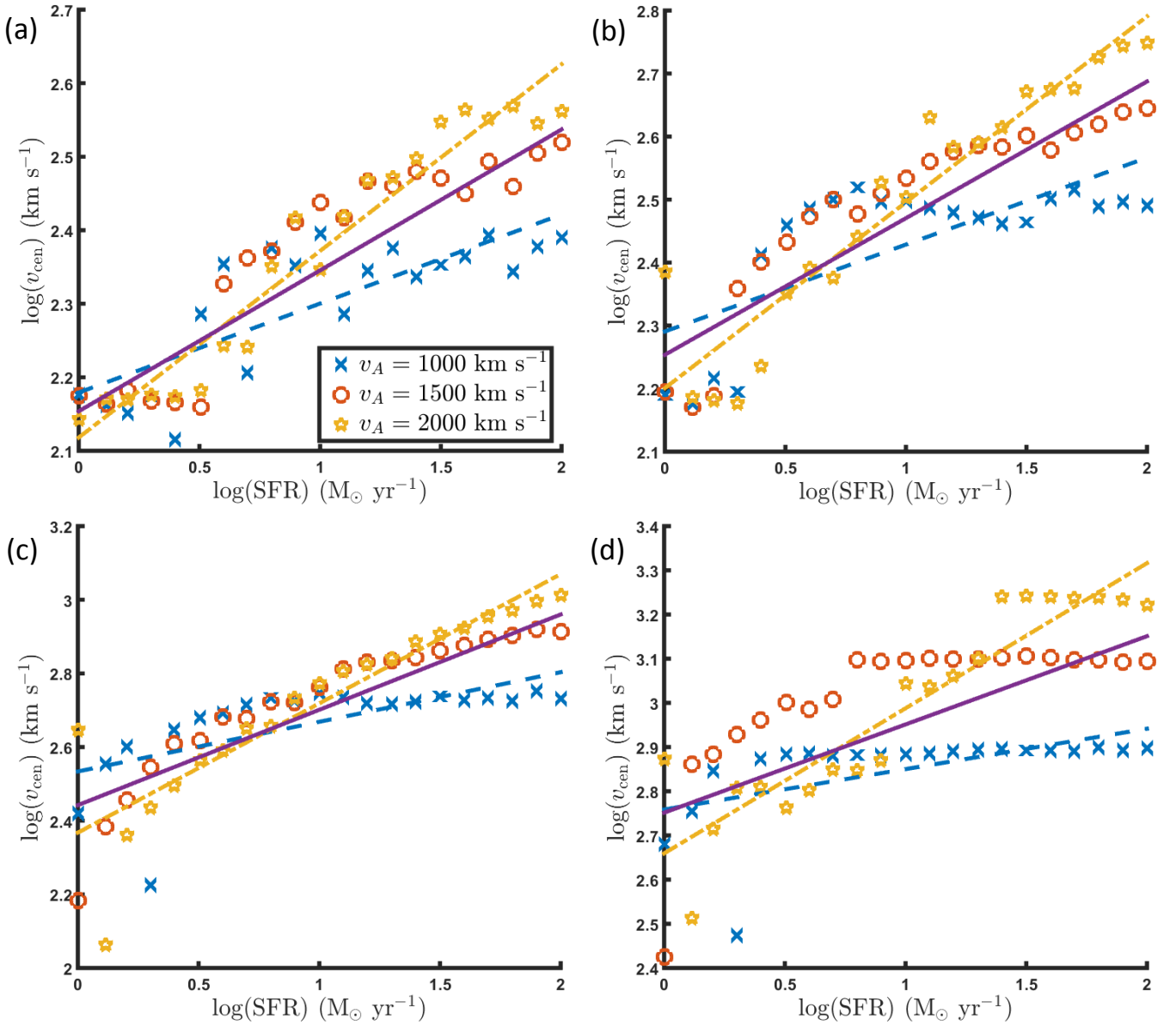

Figure 7. The v_{cen} velocity vs SFR for all S series models for select Si ions: (a) Si I, (b) Si II, (c) Si IV, (d) Si XIII. Lines indicate linear fits for models with $v_A = 2000$ km s^{-1} (yellow, dot-dash line), $v_A = 1000$ km s^{-1} (blue, dashed line), and all models together (purple, solid line).

For example, Heckman et al. (2015) calculate $\beta \approx 2$ for all of the galaxies in their sample. This would imply that the galaxies in their sample have relatively uniform v_A velocities between 1500 and 2000 km s^{-1}, putting the turnover point in the velocity vs. SFR relation high enough that it would not significantly lower their δ. When we compare the galaxy samples used we find that high δ values come from samples consisting of ULIGs (Martin 2005), high red-shift, luminous galaxies (Weiner et al. 2009), or UV-bright galaxies Heckman & Borthakur (2016). Lower δ values come from IR-bright galaxies (Rupke et al. 2005) or samples of local starburst galaxies with a variety of morphologies (Chisholm et al. 2015).

While Heckman et al. (2015) do not find a turnover in their relation between velocity and SFR, they note a turnover in the relation between velocity and $\Sigma_{\rm SFR}$ at $\sim 10^{-5}$ M$_\odot$ yr^{-1} pc^{-2}. In Heckman & Borthakur (2016) they find the turnover point to be $\sim 10^{-4}$ M$_\odot$ yr^{-1} pc^{-2}. The latter value is similar to our turnover point of $\sim 10^{-3.5}$ M$_\odot$ yr^{-1} pc^{-2} from our R series, which has a $v_A =$ 2000 km s^{-1}. We would expect their turnover point to be slightly lower because the mass loading factor of their galaxies would imply a lower v_A than our R series models. Also, we set the radius of our starburst, and from that calculate $\Sigma_{\rm SFR}$, while they find the starburst radius using the half light radius in the UV. So we would expect affect the measured turnover point in the relationship.

6. CONCLUSIONS

Using synthetic absorption lines generated from our series of 3D starburst models, we have investigated how the velocity of starburst-driven galactic winds scales with both SFR and $\Sigma_{\rm SFR}$. As implied by Equation 6 the terminal wind velocity should not depend on SFR, and by extension $\Sigma_{\rm SFR}$. Our simulations, both in this paper and in Paper I, have shown that the gas entrained in a starburst-driven wind does not move as a single coherent structure. Cold gas moves much slower than warm gas, which in turn moves slower than hot, highly ionized gas. But the relative velocities of these three gas phases do not relate to each other in a simple straight forward manner.

The measured velocity of the hot, highly ionized, gas is independent of SFR, and instead depends on v_A, and by extension, the thermalization efficiency and mass loading factor associated with the starburst. Meanwhile both the warm and cold gas scale with SFR, but only up to a point. The point where the scaling relation flattens out and the velocity becomes independent of SFR is determined again by v_A. Below this point the scaling relation is independent of v_A, and depends entirely on what temperature regime is being probed. Because of this, there is degeneracy in the velocity for different values of v_A, which means at low SFRs neutral or warm gas tracers cannot be used as proxies for the velocity of the hot, highly ionized gas. Using neutral or low ionized gas to determine outflow energetics will underestimate the total energy by an indeterminate amount. Our models show that at low SFRs it is possible to have a high velocity ($\sim$ 2000 km s^{-1}) outflow while the neutral gas embedded in the wind would have a much lower velocity ($\sim$ 300 km s^{-1}).

The relationship between the outflow velocity and $\Sigma_{\rm SFR}$ behaves in a similar way. There is a point, determined by v_A, where the relationship flattens out, but below that point the velocity scales with $\Sigma_{\rm SFR}$. The turnover has been found (Heckman et al. 2015), and is in agreement with our results. Even though we did not address how outflow velocity scales with other galaxy characteristics such as total stellar mass and the specific SFR, similar effects in the scaling relations may be present.

Our results indicate that the differences in the measured scaling relations stem from sample selection criteria that group galaxies with either a mix of v_A velocities or uniform velocities. This would explain why Rubin et al. (2014) found no correlation between the outflow velocity and either SFR and $\Sigma_{\rm SFR}$, while Chisholm et al. (2015) found a correlation for both, but with a modest slope. But Heckman et al. (2015) found a steeper slope to the correlation for both SFR and $\Sigma_{\rm SFR}$. If we only use models with a high v_A we reproduce the high slopes found by Heckman et al. (2015), and when we include models a mix of both high and low v_A we reproduce the slopes found by Chisholm et al. (2015). If we were to extend our models to include higher mass loading factors, and therefore lower v_A, our models would show no correlation, with a high scatter, as found by Rubin et al. (2014). Thus when considering the scaling relations between outflow velocity, SFR and $\Sigma_{\rm SFR}$ we cannot treat a sample of star forming galaxies as a single coherent group.

NASA Herschel grant NHSC-OT-1-1436036 and NC Space Grant supported this work.

REFERENCES

Alexandroff, R. M., Heckman, T. M., Borthakur, S., Overzier, R., & Leitherer, C. 2015, ApJ, 810, 104
Arribas, S., Colina, L., Bellocchi, E., Maiolino, R., & Villar-Martín, M. 2014, A&A, 568, A14
Bland-Hawthorn, J. 1995, PASA, 12, 190
Bordoloi, R., Lilly, S. J., Hardmeier, E., et al. 2014, ApJ, 794, 130
Chen, Y.-M., Tremonti, C. A., Heckman, T. M., et al. 2010, AJ, 140, 445
Chisholm, J., Tremonti, C. A., Leitherer, C., Chen, Y., & Wofford, A. 2016, MNRAS, 457, 3133
Chisholm, J., Tremonti, C. A., Leitherer, C., et al. 2015, ApJ, 811, 149
Cicone, C., Maiolino, R., & Marconi, A. 2016, A&A, 588, A41
Cooper, J. L., Bicknell, G. V., Sutherland, R. S., & Bland-Hawthorn, J. 2009, ApJ, 703, 330
Dahlem, M. 1997, PASP, 109, 1298
Erb, D. K., Quider, A. M., Henry, A. L., & Martin, C. L. 2012, ApJ, 759, 26
Fabbiano, G. 1988, ApJ, 330, 672
Fabbiano, G., Heckman, T., & Keel, W. C. 1990, ApJ, 355, 442
Grimes, J. P., Heckman, T., Aloisi, A., et al. 2009, ApJS, 181, 272
Heckman, T. M., Alexandroff, R. M., Borthakur, S., Overzier, R., & Leitherer, C. 2015, ApJ, 809, 147
Heckman, T. M., & Borthakur, S. 2016, ApJ, 822, 9
Heckman, T. M., Dahlem, M., Lehnert, M. D., et al. 1995, ApJ, 448, 98
Heckman, T. M., Lehnert, M. D., & Armus, L. 1993, in Astrophysics and Space Science Library, Vol. 188, The Environment and Evolution of Galaxies, ed. J. M. Shull & H. A. Thronson, 455
Heckman, T. M., Lehnert, M. D., Strickland, D. K., & Armus, L. 2000, ApJS, 129, 493
Heckman, T. M., Borthakur, S., Overzier, R., et al. 2011, ApJ, 730, 5
Ho, I.-T., Medling, A. M., Bland-Hawthorn, J., et al. 2016, MNRAS, 457, 1257
Jones, T., Stark, D. P., & Ellis, R. S. 2012, ApJ, 751, 51
Kornei, K. A., Shapley, A. E., Martin, C. L., et al. 2012, ApJ, 758, 135

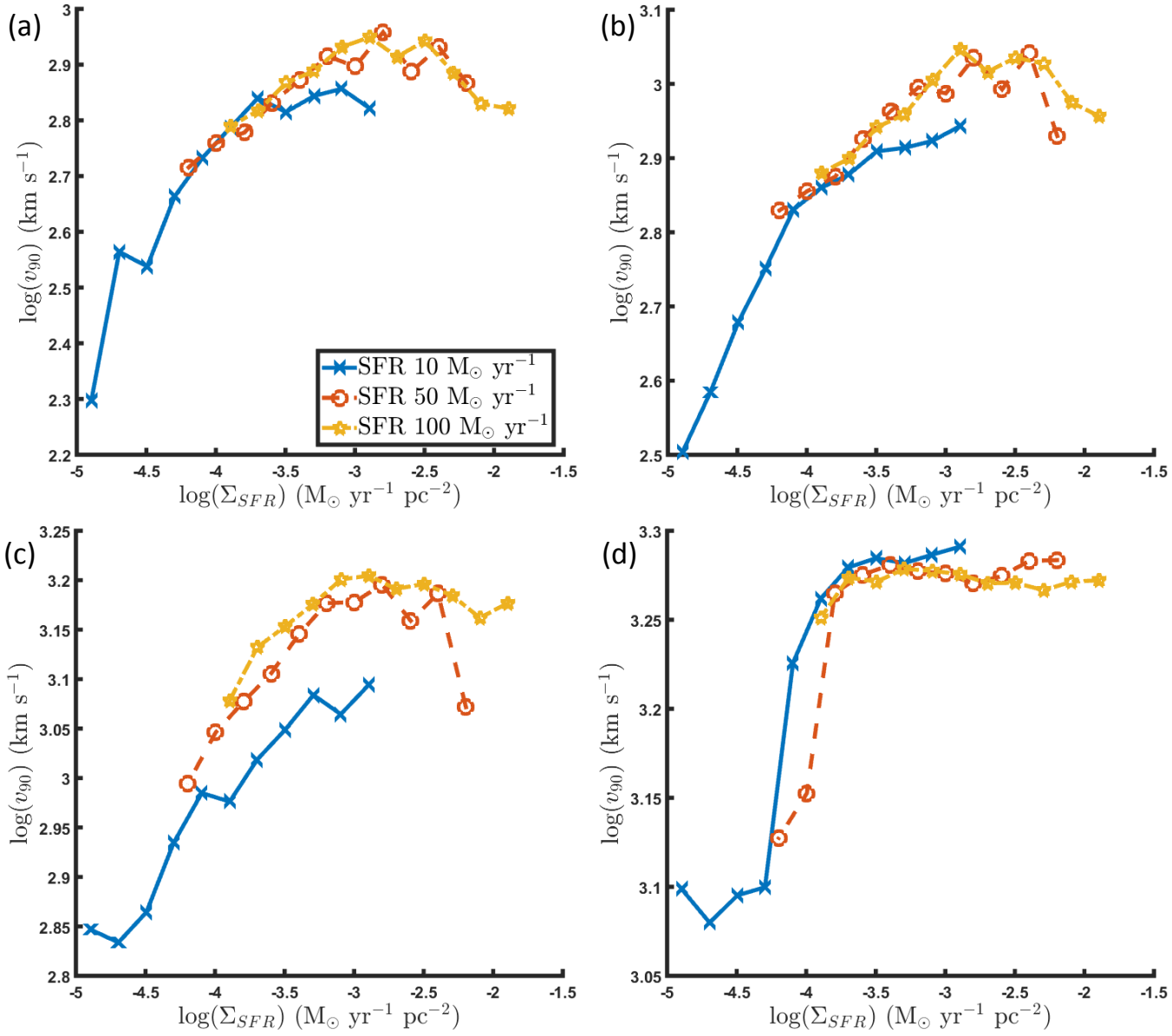

Figure 8. The v_{90} velocity vs $\Sigma_{\rm SFR}$ for all R series models for select Si ions: (a) Si I, (b) Si II, (c) Si IV, (d) Si XIII.

Kramida, A., Yu. Ralchenko, Reader, J., & and NIST ASD Team. 2015, NIST Atomic Spectra Database (ver. 5.3), [Online]. Available: http://physics.nist.gov/asd [2016, February 2]. National Institute of Standards and Technology, Gaithersburg, MD.
Kroupa, P. 2001, MNRAS, 322, 231
Kwok, S. 2007, Physics and Chemistry of the Interstellar Medium (University Science Books)
Leitherer, C., Schaerer, D., Goldader, J. D., et al. 1999, ApJS, 123, 3
Martin, C. L. 2005, ApJ, 621, 227
Martin, C. L., Shapley, A. E., Coil, A. L., et al. 2012, ApJ, 760, 127
Mazzotta, P., Mazzitelli, G., Colafrancesco, S., & Vittorio, N. 1998, A&AS, 133, 403
Rubin, K. H. R., Prochaska, J. X., Koo, D. C., et al. 2014, ApJ, 794, 156
Rupke, D. S., Veilleux, S., & Sanders, D. B. 2005, ApJS, 160, 115
Schreier, F. 2011, Journal of Quantitative Spectroscopy and Radiative Transfer, 112, 1010
Stone, J. M., Gardiner, T. A., Teuben, P., Hawley, J. F., & Simon, J. B. 2008, ApJS, 178, 137
Strickland, D. K., & Heckman, T. M. 2009, ApJ, 697, 2030
Strickland, D. K., & Stevens, I. R. 2000, MNRAS, 314, 511
Tanner, R., Cecil, G., & Heitsch, F. 2016, ApJ, 821, 7
Veilleux, S., Cecil, G., & Bland-Hawthorn, J. 2005, ARA&A, 43, 769
Watson, M. G., Stanger, V., & Griffiths, R. E. 1984, ApJ, 286, 144
Weiner, B. J., Coil, A. L., Prochaska, J. X., et al. 2009, ApJ, 692, 187
Wofford, A., Leitherer, C., & Salzer, J. 2013, ApJ, 765, 118